

THE BURST MODE OF ACCRETION AND DISK FRAGMENTATION IN THE EARLY EMBEDDED STAGES OF STAR FORMATION

EDUARD I. VOROBYOV^{1,2} AND SHANTANU BASU³

Accepted for publication by The Astrophysical Journal

ABSTRACT

We revisit our original papers on the burst mode of accretion by incorporating a detailed energy balance equation into a thin-disk model for the formation and evolution of circumstellar disks around low-mass protostars. Our model includes the effect of radiative cooling, viscous and shock heating, and heating due to stellar and background irradiation. Following the collapse from the prestellar phase allows us to model the early embedded phase of disk formation and evolution. During this time, the disk is susceptible to fragmentation, depending upon the properties of the initial prestellar core. Globally, we find that higher initial core angular momentum and mass content favors more fragmentation, but higher levels of background radiation can moderate the tendency to fragment. A higher rate of mass infall onto the disk than that onto the star is a necessary but not sufficient condition for disk fragmentation. More locally, both the Toomre Q -parameter needs to be below a critical value *and* the local cooling time needs to be shorter than a few times the local dynamical time. Fragments that form during the early embedded phase tend to be driven into the inner disk regions, and likely trigger mass accretion and luminosity bursts that are similar in magnitude to FU-Orionis-type or EX-Lupi-like events. Disk accretion is shown to be an intrinsically variable process, thanks to disk fragmentation, nonaxisymmetric structure, and the effect of gravitational torques. The additional effect of a generic α -type viscosity acts to reduce burst frequency and accretion variability, and is likely to not be viable for values of α significantly greater than 0.01.

Subject headings: accretion, accretion disks—hydrodynamics—instabilities—ISM: clouds—stars: formation

1. INTRODUCTION

Typical rotation rates of $\sim 1 \text{ km s}^{-1} \text{ pc}^{-1} \approx 10^{-14} \text{ rad s}^{-1}$ measured in molecular cloud cores (Goodman et al. 1993; Caselli et al. 2002) are sufficient to provide a significant angular momentum barrier to star formation. Most of the infalling matter will land on a protostellar disk rather than directly onto a protostar, since magnetic braking is rendered ineffective by ohmic dissipation in the near-stellar environment. Therefore, the early phase of disk formation and evolution holds the key to understanding stellar mass accumulation, and sets the initial conditions for a later stage of disk evolution during which planets may form by core accretion (Lissauer 1993). The early disk phase is characterized by episodic accretion, as predicted theoretically in our earlier papers (Vorobyov & Basu 2005, 2006) and inferred observationally by compiling luminosity distributions of young stellar objects (Enoch et al. 2009). Furthermore, the FU Orionis stars, named after the prototype FU Ori (Herbig 1977), provide direct evidence of transient luminosity variations (3 – 6 mag during $\leq 100 \text{ yr}$). These luminosity bursts have been associated with a sharp increase of the mass accretion rate onto the protostar (Hartmann & Kenyon 1996) and various physical mechanisms have been proposed to explain this phenomenon (see e.g., Lin & Papaloizou 1985; Bonnell & Bastein 1992;

Bell & Lin 1994; Armitage et al. 2001; Lodato & Clarke 2004; Vorobyov & Basu 2005, 2006; Pfalzner et al. 2008; Zhu et al. 2009, 2010; Forgan & Rice 2010; Bate 2010).

Our earlier calculations (Vorobyov & Basu 2005, 2006, 2007, 2008) have revealed the importance of studying disk evolution using a self-consistent method of following the collapse of an initial prestellar core. Disk formation occurs after a central stellar core has formed, but the disk continues to gain mass from the surrounding infalling envelope. Under certain conditions, this leads to disk fragmentation and the development of the “burst mode” of accretion, during which fragments are driven onto the protostar and episodic high mass accretion events actually account for the majority of mass accumulation onto the protostar. For example, Fig. 1 of Vorobyov & Basu (2007) and Vorobyov (2009b) reveals the correlation of the burst mode with infall from the envelope onto the disk. The above models were characterized by a large dynamic range of spatial *and* temporal scales, so that core collapse from $\sim 10^4 \text{ AU}$ scales down to an inner sink cell of size 5 – 10 AU was resolved, and the evolution followed for up to several Myr *after* the formation of a central protostar. Aside from the initial discovery of the burst mode, long-term evolution revealed that, even after the burst mode ceases, the disk settles into a self-regulated mode in which the Toomre- Q parameter stays near the critical value. In this phase, residual accretion due to gravitational torques (resulting from persistent low-amplitude nonaxisymmetric structure driven by the swing amplifier effect) occurs at a rate that can explain observed T Tauri star mass accretion (Vorobyov & Basu 2007, 2008), but with late time disk masses that are about an order of magnitude

¹ Institute for Computational Astrophysics, Saint Mary’s University, Halifax, NS B3H 3C3, Canada; vorobyov@ap.smu.ca.

² Research Institute of Physics, Southern Federal University, Stachki 194, Rostov-on-Don, 344090, Russia.

³ Department of Physics and Astronomy, The University of Western Ontario, London, ON N6A 3K7, Canada; basu@uwo.ca.

greater than observational estimates (Vorobyov 2009a) which may really represent lower limits to the actual values (see e.g., Andrews & Williams 2007). The effect of additional angular momentum transport due to an α -viscosity was explored by Vorobyov & Basu (2009a,b), with a finding that such an α would likely lie in the range $10^{-3} - 10^{-2}$ to satisfy observational and theoretical constraints. An α -viscosity in this range could begin to dominate gravitational torques only during the late evolution (Class II, or T Tauri phase) and yield a late time accretion rate that was a factor 2 – 3 greater than that due to gravitational torques alone. Values of α well above this range were found to lead to a lack of accretion variability in the early stages, and quickly lead to very low mass disks, but with disk lifetimes ≤ 1 Myr that may be too short.

The above calculations employed a barotropic equation of state, which captured the basic features of the transition from isothermal to polytropic evolution at high densities (at number density $n \gtrsim 10^{11} \text{ cm}^{-3}$), as seen in spherical radiative transfer calculations (Masunaga & Inutsuka 2000). However, such calculations could not capture the detailed thermodynamics in the vicinity of forming clumps. That can be a crucial effect in the development of a clump, including determining whether it can even form at all (Gammie 2001; Rice et al. 2003; Mejía et al. 2005; Cai et al. 2008). Hence, a criticism of the above modeling has been that the clump formation and consequent burst mode may not be a robust result in the case of more realistic thermodynamics. We note that Vorobyov & Basu (2006) were aware of this difficulty, and tested out models with high values of polytropic index such that the temperatures for densities $n \gtrsim 10^{11}$ exceeded that found in radiative transfer calculations. The clump formation and bursts still occurred in those cases, thanks to significant forcing by mass accretion onto the disk during the early phases, although their number and frequency could be strongly reduced. Bursts were found to be robust in the context of those models, but their frequency depended strongly on thermal evolution as well as the mass and angular momentum content of infalling material.

In this paper, we have made a major improvement by implementing the energy balance equation, which includes radiative cooling, viscous and shock heating, and heating due to stellar and background irradiation. We continue to include angular momentum transport due to a generic α -viscosity term, since mechanisms other than gravitational torques may be at work. Numerical resolution is also extended to greater values than in our original papers on the burst mode (Vorobyov & Basu 2005, 2006). An important question is: will the existence of the burst mode be robust under these circumstances, and what will be its properties? We address these questions in Sections 3 – 5. A description of our model is in Section 2, and we provide extended discussion of the model features in Section 6. A summary of results is in Section 7.

2. DESCRIPTION OF THE NUMERICAL MODEL

The main concepts of our numerical approach are explained in detail in Vorobyov & Basu (2006). Here we review some main properties and focus mainly on the implementation of radiative cooling, viscous and shock

heating, and heating due to stellar and background irradiation.

We start our numerical integration in the pre-stellar phase, which is characterized by a collapsing *starless* cloud core, continue into the embedded phase of star formation (hereafter, EPSF), during which a star, disk, and envelope are formed, and terminate our simulations in the T Tauri phase, when most of the envelope has accreted onto the forming star/disk system. In the EPSF, the disk occupies the innermost region of our numerical grid, while the larger outer part of the grid is taken up by the infalling envelope, which is a remnant of the parent cloud core. This ensures that the protostellar disk is not isolated in the EPSF but is subject to intense mass loading from the envelope. In addition, the mass accretion rate onto the disk \dot{M}_{env} is not a free parameter of the model but is self-consistently determined by the gas dynamics in the envelope.

We introduce a “sink cell” at $r_{\text{sc}} = 6$ AU and impose a free inflow inner boundary condition. We monitor the gas surface density in the sink cell and when its value exceeds a critical value for the transition from isothermal to adiabatic evolution, we introduce a central point-mass star. In the subsequent evolution, 90% of the gas that crosses the inner boundary is assumed to land onto the central star plus the inner axisymmetric disk at $r < 6$ AU. This inner disk is dynamically inactive, it contributes only to the total gravitational potential and is used to secure a smooth behavior of the gravity force down to the stellar surface. The other 10% of the accreted gas is assumed to be carried away with protostellar jets. The latter are triggered only after the formation of the central star. The fact that we use a sink cell means that our model cannot resolve the formation of binary (or multiple) stellar (or planetary) systems on spatial scales smaller than the size of the sink cell.

2.1. Basic equations

We make use of the thin-disk approximation to compute the gravitational collapse of rotating, gravitationally unstable cloud cores. This approximation is an excellent means to calculate the evolution for many orbital periods and many model parameters and its justification is provided in Appendix A. We note that in the thin-disk approximation all material from the envelope lands onto the outer disk regions. This is however a reasonable assumption according to Visser et al. (2009), who accurately calculated the gas trajectories in the infalling envelope and found that the bulk of the infalling material landed onto the disk’s outer edge.

The basic equations of mass, momentum, and energy transport in the thin-disk approximation are

$$\frac{\partial \Sigma}{\partial t} = -\nabla_p \cdot (\Sigma \mathbf{v}_p), \quad (1)$$

$$\frac{\partial}{\partial t} (\Sigma \mathbf{v}_p) + [\nabla \cdot (\Sigma \mathbf{v}_p \otimes \mathbf{v}_p)]_p = -\nabla_p \mathcal{P} + \Sigma \mathbf{g}_p + (\nabla \cdot \mathbf{\Pi})_p, \quad (2)$$

$$\frac{\partial e}{\partial t} + \nabla_p \cdot (e \mathbf{v}_p) = -\mathcal{P}(\nabla_p \cdot \mathbf{v}_p) - \Lambda + \Gamma + (\nabla \mathbf{v})_{pp'} : \Pi_{pp'}, \quad (3)$$

where subscripts p and p' refers to the planar components (r, ϕ) in polar coordinates, Σ is the mass surface density,

e is the internal energy per surface area, $\mathcal{P} = \int_{-Z}^Z P dz$ is the vertically integrated form of the gas pressure P , Z is the radially and azimuthally varying vertical scale height determined in each computational cell using an assumption of local hydrostatic equilibrium (Vorobyov & Basu 2009a), $\mathbf{v}_p = v_r \hat{\mathbf{r}} + v_\phi \hat{\boldsymbol{\phi}}$ is the velocity in the disk plane, $\mathbf{g}_p = g_r \hat{\mathbf{r}} + g_\phi \hat{\boldsymbol{\phi}}$ is the gravitational acceleration in the disk plane, and $\nabla_p = \hat{\mathbf{r}} \partial / \partial r + \hat{\boldsymbol{\phi}} r^{-1} \partial / \partial \phi$ is the gradient along the planar coordinates of the disk. The planar components of the divergence of the stress tensor $(\nabla \cdot \mathbf{\Pi})_p$, symmetrized velocity gradient tensor $(\nabla \mathbf{v})_p$, viscous heating $(\nabla \mathbf{v})_{pp'} : \mathbf{\Pi}_{pp'}$, and symmetric dyadic $\Sigma \mathbf{v}_p \otimes \mathbf{v}_p$ are found according to the usual rules (see Appendix C).

The gravitational acceleration \mathbf{g}_p includes the gravity of a central point-mass star (when formed), the gravity of an inner disk ($r < r_{\text{sc}}$), and the self-gravity of a circumstellar disk and envelope. The latter component is found by solving for the Poisson integral

$$\Phi(r, \phi) = -G \int_{r_{\text{sc}}}^{r_{\text{out}}} r' dr' \times \int_0^{2\pi} \frac{\Sigma(r', \phi') d\phi'}{\sqrt{r'^2 + r^2 - 2rr' \cos(\phi' - \phi)}}, \quad (4)$$

where r_{out} is the radial position of the computational outer boundary, or, equivalently, is the initial radius of a cloud core. This integral is calculated using a FFT technique which applies the 2D Fourier convolution theorem for polar coordinates (see Binney & Tremaine 1987, Sect. 2.8).

2.2. Viscosity

Viscosity in circumstellar disks may be an important source of mass and angular momentum transport and heat production. The best candidate to date is turbulent viscosity induced by the magneto-rotational instability (Balbus & Hawley 1991), though other mechanisms such as nonlinear hydrodynamic turbulence cannot be completely eliminated due to the large Reynolds numbers involved. We make no specific assumptions about the source of turbulence and parameterize the magnitude of kinematic viscosity using a modified form of the α -prescription

$$\nu = \alpha c_s Z \mathcal{F}_\alpha(r), \quad (5)$$

where $c_s^2 = \gamma \mathcal{P} / \Sigma$ is the square of effective sound speed calculated at each time step from the model's known \mathcal{P} and Σ . The function $\mathcal{F}_\alpha(r) = 2\pi^{-1} \tan^{-1} [(r_d/r)^{10}]$ is a modification to the usual α -prescription of Shakura & Sunyaev (1973) that guarantees that the turbulent viscosity operates only in the disk and quickly reduces to zero beyond the disk radius r_d . The latter is determined using a typical density for the disk to envelope transition, $\Sigma_{d2e} = 0.1 \text{ g cm}^{-2}$, and the radial gas velocity (see Vorobyov 2010, for details).

In this paper, we use a spatially and temporally uniform α , with its value set to 0.005 in most models. This choice is based on our recent work (Vorobyov & Basu 2009a), wherein we have studied numerically the secular evolution of viscous and self-gravitating disks. We found that *if* circumstellar disks around solar-mass protostars

could generate and sustain turbulence, then the temporally and spatially averaged α should lie in the range $10^{-3} - 10^{-2}$. Smaller values of α ($\lesssim 10^{-4}$) have little effect on the resultant disk structure and mass accretion history, which, in this case, is totally controlled by disk gravity. Larger values ($\alpha \gtrsim 10^{-1}$) destroy circumstellar disks during less than 1.0 Myr of evolution and are thus inconsistent with mean disk lifetimes of the order of 2–3 Myr. Nevertheless, α may vary in time and have greater values in the EPSF (the duration of which is usually much shorter than 1 Myr). The effect of varying α is briefly discussed in Section 5.3.

Viscosity enters the basic equations via the viscous stress tensor $\mathbf{\Pi}$ expressed as

$$\mathbf{\Pi} = 2\Sigma \nu \left(\nabla \mathbf{v} - \frac{1}{3} (\nabla \cdot \mathbf{v}) \mathbf{e} \right), \quad (6)$$

where \mathbf{e} is the unit tensor. We note that we take no simplifying assumptions about the form of $\mathbf{\Pi}$ apart from those imposed by the adopted thin-disk approximation.

2.3. Energy balance

Equation (3) for the internal energy balance includes the usual compressional term $\mathcal{P} (\nabla_p \cdot \mathbf{v}_p)$, radiative cooling Λ , heating due to stellar/background irradiation Γ , and viscous heating $(\nabla \mathbf{v})_{pp'} : \mathbf{\Pi}_{pp'}$. We assume that the heat generated in the disk interior due to viscosity and shocks is transported to the disk surface by radiation, which escapes from the disk surface at a rate per unit area $2\sigma T_{\text{eff}}^4$. This means that we neglect other possible sources of heat transport such as convection. We then make use of the diffusion approximation and link the effective surface temperature T_{eff} with the mid-plane temperature of gas T_{mp} via the following relation $T_{\text{eff}}^4 = 8T_{\text{mp}}^4/(3\tau)$, where τ is the optical depth (Hubeny 1990; Johnson & Gammie 2003). Finally, we substitute τ^{-1} with $\tau/(1 + \tau^2)$ to allow for a smooth transition between the optically thick and optically thin regimes (Johnson & Gammie 2003). The resulting cooling function is described as

$$\Lambda = \mathcal{F}_c \sigma T_{\text{mp}}^4 \frac{\tau}{1 + \tau^2}, \quad (7)$$

where σ is the Stefan-Boltzmann constant and $\mathcal{F}_c = 2 + 20 \tan^{-1}(\tau)/(3\pi)$ is a function that secures a correct transition between the cooling function in the optically thick regime $\Lambda_{\text{thick}} = 16\sigma T_{\text{mp}}^4/(3\tau)$ and the optically thin one $\Lambda_{\text{thin}} = 2\sigma T_{\text{mp}}^4 \tau$. We use frequency-integrated opacities of Bell & Lin (1994), which are smoothed at the principal opacity transitions to allow for iterative solution methods to converge quickly.

Heating due to stellar and background irradiation is treated assuming that this process operates in the opposite direction to that of radiative cooling, i.e., radiation from the central star and natal molecular cloud hits the surface and diffuses down to the midplane where it transforms into heat. This allows us to express the heating function as

$$\Gamma = \mathcal{F}_c \sigma T_{\text{irr}}^4 \frac{\tau}{1 + \tau^2}, \quad (8)$$

where T_{irr} is the irradiation temperature at the disk surface determined by the stellar and background black-body irradiation as

$$T_{\text{irr}}^4 = T_{\text{bg}}^4 + \frac{F_{\text{irr}}(r)}{\sigma}, \quad (9)$$

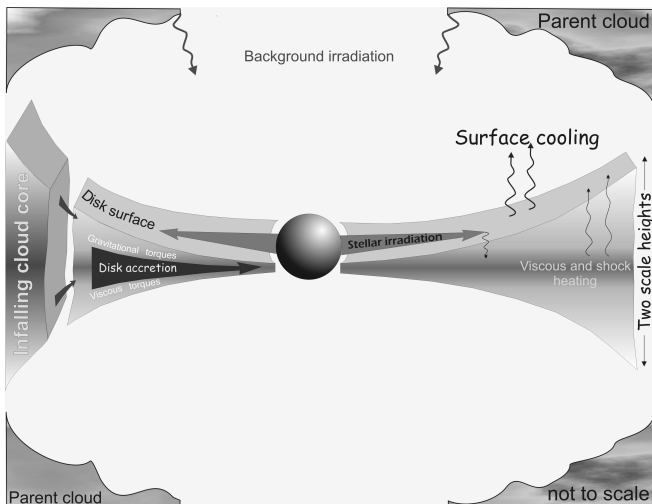


FIG. 1.— Schematic representation of the numerical model. See the text for a detailed explanation.

where T_{bg} is the uniform background temperature (in our model set to the initial temperature of the natal cloud core) and $F_{irr}(r)$ is the radiation flux (energy per unit time per unit surface area) absorbed by the disk surface at radial distance r from the central star. The latter quantity is calculated as

$$F_{irr}(r) = A_{irr} \frac{L_*}{4\pi r^2} \cos \gamma_{irr}, \quad (10)$$

where L_* is the stellar luminosity, γ_{irr} is the incidence angle of radiation arriving at the disk surface at radial distance r , and A_{irr} is a time-dependent factor that accounts for the attenuation of stellar radiation in the EPSF (see Appendix B for more details).

The stellar luminosity L_* is the sum of the accretion luminosity $L_{accr} = GM_*\dot{M}/(2r_*)$ arising from the gravitational energy of accreted gas and the photospheric luminosity L_{ph} due to gravitational compression and deuterium burning in the star interior. The stellar mass M_* and accretion rate onto the star \dot{M} are determined self-consistently during numerical simulations via the amount of gas passing through the sink cell. The stellar radius r_* is calculated using an approximation formula of Palla & Stahler (1991), modified to take into account the formation of the first molecular core (Masunaga & Inutsuka 2000). More specifically, we assume that during 2×10^4 yr after the formation of the central protostar, the stellar radius is $r_* = 5$ AU. Then, the second atomic core forms and the stellar radius is determined as

$$r_* = \begin{cases} 2.5 R_\odot & M_* \leq 0.4 M_\odot, \\ 2.5 + 4.2(M_* - 0.4) R_\odot & 0.4 M_\odot < M_* \leq 1.0 M_\odot, \\ 5.0 R_\odot & M_* > 1.0 M_\odot. \end{cases} \quad (11)$$

Transition between these two modes is smoothed over a period of 0.5×10^4 yr.

The photospheric luminosity L_{ph} is taken from the pre-main sequence tracks for the low-mass stars and brown dwarfs calculated by D'Antona & Mazitelli (1997). Unfortunately, the stellar age in these tracks is difficult to relate with the actual physical evolution time in numerical simulations of gravitational collapse. A common practice starting from Myers et al. (2005) is to add t_{offset}

to the times of the pre-main sequence tracks to account for the delay between the onset of cloud core collapse and the zero-time of these tracks. Indeed, after collapse begins, the forming star must wait for some time before the luminosity due to contraction and deuterium burning (as described by D'Antona & Mazitelli (1997)) will begin. The exact value of t_{offset} is however uncertain because it would certainly depend on the initial conditions in a cloud core such as the gas temperature, density enhancement, strength of magnetic fields, etc.

Fortunately, we accurately follow the pre-stellar collapse phase and can actually determine the time t_{fc} that it takes for a cloud core to reach an optically thick density of order 10^{11} cm^{-3} in its interior and start forming the first (molecular) hydrostatic core. We then assume that the zero-time of D'Antona & Mazitelli's tracks corresponds to the onset of the formation of the second atomic core t_{sc} , which follows the formation of the first core after approximately 2×10^4 yr (Masunaga & Inutsuka 2000). With these assumptions in mind, the photospheric luminosity $L_{*,ph}$ is set to zero for $t < t_{s.c.} = t_{f.c.} + 2 \times 10^4$ yr and then is calculated according to D'Antona & Mazitelli (1997) with the zero-time of their tracks corresponding to $t_{s.c.}$ in our numerical simulations. We note that the D'Antona & Mazitelli's tracks do not cover the very early phases of stellar evolution. Therefore, we have used a power-law expression to extrapolate to times earlier than those included in the pre-main sequence tracks, $L_{ph} = L_{ph,0}(t/t_0)^4$, where t_0 is the earliest time in the tracks and $L_{ph,0}$ is the pre-main sequence luminosity at this time.

Viscous heating operates in the disk interior and is calculated using the standard expression $(\nabla \mathbf{v})_{pp'} : \mathbf{\Pi}_{pp'}$ (see Appendix C). We note that we use the most general expression for viscous heating and take none of the popular simplifying assumptions (such as disk axisymmetry) apart from those imposed by the thin-disk approximation. Heating due to shock waves is taken into account via compressional heating $\mathcal{P}(\nabla_p \cdot \mathbf{v}_p)$ and artificial viscosity. The latter is implemented in the code using the standard prescription of Richtmyer & Morton (1957). The gas pressure \mathcal{P} and internal energy per surface area e are related via the ideal gas law $\mathcal{P} = (\gamma - 1)e$, with the ratio of specific heats $\gamma = 7/5$. A more detailed approach would be to implement a variable γ as in e.g. Forgan et al. (2009). However, a rigorous realization of this mechanism requires calculating the excitation levels of main atomic and molecular coolants and is beyond the limits of the current paper. We explored the effect of varying γ in our previous paper in the context of polytropic disks (Vorobyov & Basu 2006) and showed that the $\gamma = 5/3$ case was usually characterized by disks less prone to fragmentation.

In Figure 1 we summarize our model by drawing a schematic picture of the main model ingredients in the EPSF. A central star is surrounded by a disk which accretes matter from a collapsing natal cloud core. The infalling material lands onto the disk outer edge and is transported toward to the inner disk boundary by a combined action of gravitational and viscous torques. Mass accretion onto the star, along with stellar compression and deuterium burning, give rise to stellar irradiation, part of which is absorbed by the flaring disk surface and is transformed into heat in the disk interior. Another

TABLE 1
MODEL PARAMETERS

| Model | β | Ω_0 | r_0 | M_{cl} | T_{bg} | α |
|------------------------|----------------------|------------|-------|-----------------|-----------------|--------------------|
| reference | 1.3×10^{-2} | 2.7 | 1540 | 0.70 | 10 | 5×10^{-3} |
| lower- β | 2.8×10^{-3} | 1.2 | 1640 | 0.73 | 10 | 5×10^{-3} |
| $M_{\text{cl}} = 0.16$ | 1.3×10^{-2} | 12 | 340 | 0.16 | 10 | 5×10^{-3} |
| $M_{\text{cl}} = 0.23$ | 1.3×10^{-2} | 8 | 514 | 0.23 | 10 | 5×10^{-3} |
| $M_{\text{cl}} = 0.92$ | 1.3×10^{-2} | 2 | 2060 | 0.92 | 10 | 5×10^{-3} |
| $T_{\text{bg}} = 10$ | 1.3×10^{-2} | 1.8 | 2780 | 1.2 | 10 | 5×10^{-3} |
| $T_{\text{bg}} = 20$ | 1.3×10^{-2} | 4.8 | 1200 | 1.1 | 20 | 5×10^{-3} |
| $T_{\text{bg}} = 30$ | 1.2×10^{-2} | 8.2 | 860 | 1.15 | 30 | 5×10^{-3} |
| $\alpha = 0$ | 1.3×10^{-2} | 2.7 | 1540 | 0.70 | 10 | 0 |
| $\alpha = 0.05$ | 1.3×10^{-2} | 2.7 | 1540 | 0.70 | 10 | 5×10^{-2} |

NOTE. — All masses are in M_{\odot} , temperatures in Kelvin, distances in AU, and angular velocities in $\text{km s}^{-1} \text{pc}^{-1}$.

source of external heating is the background irradiation from the natal molecular cloud. The heat generated in the disk interior by viscosity and shocks is transported to the disk surface by radiation. The latter escapes from the disk surface giving rise to the only global cooling mechanism in our model.

2.4. Solution procedure

Equations (1)–(3) are solved in polar coordinates (r, ϕ) on a numerical grid with 512×512 grid zones. The radial points are logarithmically spaced. The innermost grid point is located at the position of the sink cell $r_{\text{sc}} = 6$ AU, and the size of the first adjacent cell varies in the 0.07–0.1 AU range depending on the cloud core size. This corresponds to a radial resolution $\Delta r = 1.1$ –1.6 AU at 100 AU. The outer boundary is reflecting.

We use the method of finite differences with a time-explicit solution procedure similar in methodology to the ZEUS code (Stone & Norman 1992). The advection is treated using the van Leer interpolation scheme. It is well known that cooling and heating time scales may become much shorter than the dynamical time scale, which would result in prohibitively small time steps. Therefore, the update of the internal energy per surface area e due to cooling Λ and heating Γ is done implicitly using the Newton-Raphson method of root finding, complemented by the bisection method where the Newton-Raphson iterations fail to converge. The accuracy is guaranteed by not allowing e to change more than 30% over one time step. If this condition is violated in a particular cell, we employ subcycling for this cell, i.e., the solution is sought with a local time step that is smaller than the global time step by a factor of 2. The local time step may be further decreased until the desired accuracy is reached.

The viscous force and heating terms in Equations (2) and (3) are implemented in the code using an explicit finite-difference scheme. This is found to be adequate for $\alpha \lesssim 0.01$ because other terms (usually, the azimuthal advection) dominate in the Courant condition that controls the time step. However, for higher values of α we find that the viscous terms start to impose strict time step limitations and an implicit scheme is desirable in order to extend numerical simulations to the Class II phase of stellar evolution. A small amount of artificial viscosity is added to the code to smooth out shocks. The associated artificial viscosity torques integrated over the disk area are negligible in comparison with gravitational torques. Occasionally, however, the shocks may become strong

enough to impose strict limitations on the Courant condition, which results in a considerable decrease in the time step of integration. In this case, we use subcycling in the same manner as we do for the internal energy update due to cooling/heating.

2.5. Initial conditions

Initially, cloud cores have surface densities Σ and angular velocities Ω typical for a collapsing, axisymmetric, magnetically supercritical core (Basu 1997):

$$\Sigma = \frac{r_0 \Sigma_0}{\sqrt{r^2 + r_0^2}}, \quad (12)$$

$$\Omega = 2\Omega_0 \left(\frac{r_0}{r} \right)^2 \left[\sqrt{1 + \left(\frac{r}{r_0} \right)^2} - 1 \right], \quad (13)$$

where Ω_0 is the central angular velocity and r_0 is the radius of central near-constant-density plateau defined as $r_0 = \sqrt{A c_s^2 / (\pi G \Sigma_0)}$. We note that the above form of the column density is very similar to the integrated column density of a Bonnor-Ebert sphere (Dapp & Basu 2009). Furthermore, equation (12) at large radii $r \gg r_0$ leads to the gas volume density distribution $\rho = A c_s^2 / (2\pi G r^2)$, if it is integrated in the vertical direction assuming a local vertical hydrostatic equilibrium, i.e., $\rho = \Sigma / (2Z)$ and $Z = c_s^2 / (\pi G \Sigma)$. This means that our initial gas surface density configuration can be considered to have a factor of A positive density enhancement compared to that of the singular isothermal sphere $\rho_{\text{sis}} = c_s^2 / (2\pi G r^2)$ (Shu 1977). Throughout the paper, we use $A = 1.2$.

Cloud cores are also characterized by the ratio of rotational to gravitational energy $\beta = E_{\text{rot}} / |E_{\text{grav}}|$, where the rotational and gravitational energies are calculated as

$$E_{\text{rot}} = 2\pi \int_{r_{\text{sc}}}^{r_{\text{out}}} r a_c \Sigma r dr, \quad E_{\text{grav}} = -2\pi \int_{r_{\text{sc}}}^{r_{\text{out}}} r g_r \Sigma r dr. \quad (14)$$

Here, $a_c = \Omega^2 r$ is the centrifugal acceleration, and r_{out} is the outer cloud core radius. The adopted values of β lie within the limits inferred by Caselli et al. (2002) for dense molecular cloud cores, $\beta = (10^{-4} - 0.07)$. Cloud cores are initially isothermal, with the uniform gas temperature taking values between $T_{\text{init}} = 10$ K and 30 K, depending on the model. In addition, every model core is characterized by a distinct ratio $r_{\text{out}}/r_0 = 6$ in order to generate gravitationally unstable truncated cores of similar form.

For the in-depth analysis, we consider a model with $M_{\text{cl}} = 0.7 M_{\odot}$, $\beta = 1.3 \times 10^{-2}$, $A = 1.2$, $\alpha = 5 \times 10^{-3}$ (the viscous α -parameter), and $T_{\text{init}} = 10$ K. These and other model parameters are summarized in Table 1. This model (hereafter, the reference model) is chosen solely because it best represents the main characteristics of disk fragmentation in the embedded phase of star formation. Other models will be introduced as the need arises.

3. GRAVITATIONAL INSTABILITY AND DISK FRAGMENTATION

Theoretical and numerical studies of the evolution of protostellar disks indicate that disk fragmentation is a complicated phenomenon, which can be influenced by

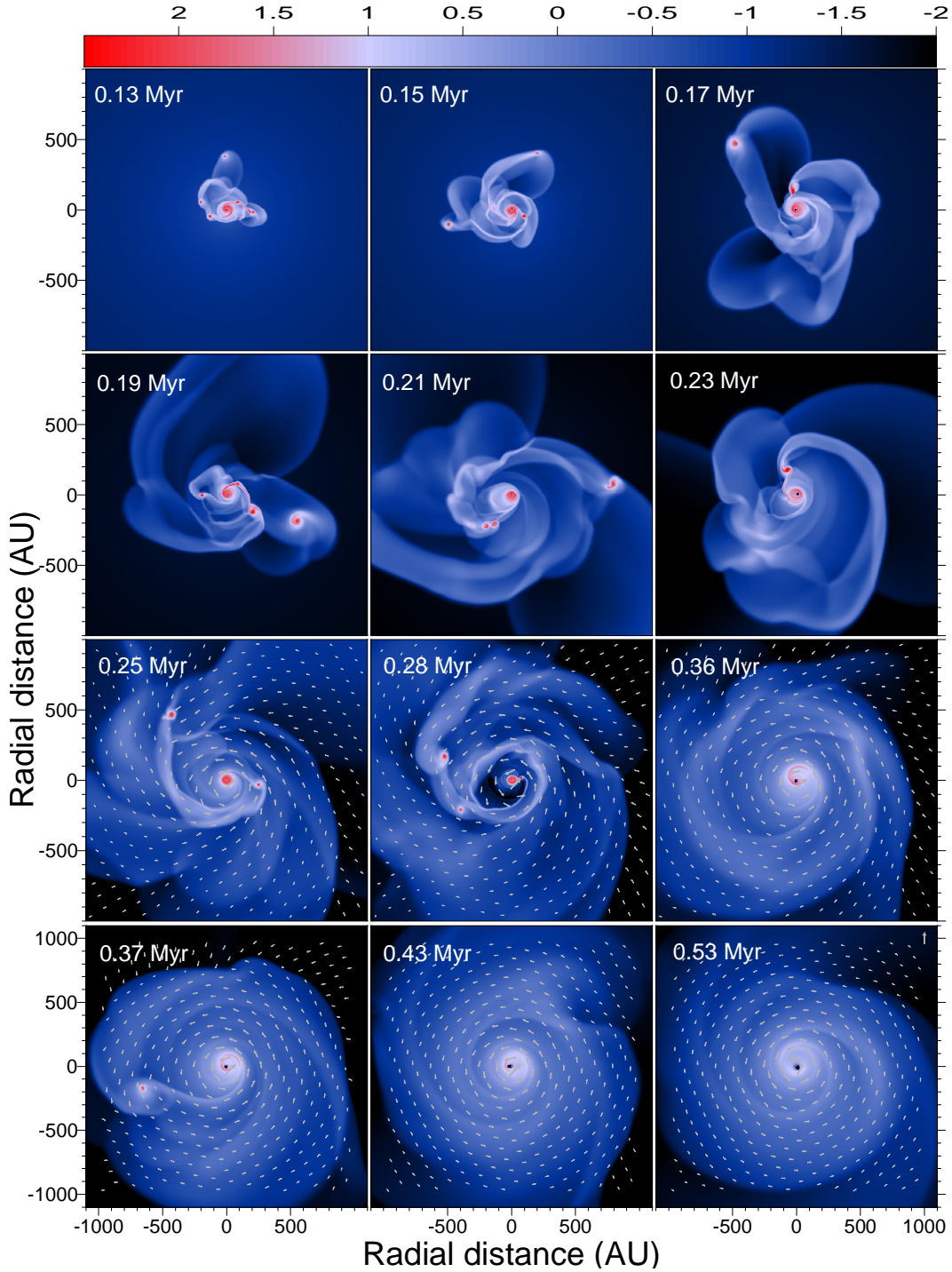


FIG. 2.— Gas surface density distribution (g cm^{-2} , log units) in the reference model at several time instances after the formation of the central star (located in the coordinate center). Two bottom rows also shows a gas velocity field superimposed onto the surface density distribution. The vertical arrow in the bottom-right panel has a dimension of 5 km s^{-1} .

both the internal disk physics and external environment. The latter may influence the disk susceptibility to fragmentation directly (through, e.g., disk irradiation) or indirectly by setting the initial conditions in cloud cores that favor or disfavor fragmentation in subsequently formed disks. The following four criteria for disk fragmentation are best studied and their significance is well established.

1. The ratio of the local cooling time $t_c = e/\Lambda$ to the local dynamical time Ω^{-1} is smaller than a

few, i.e., $t_c \Omega \leq C$ (Gammie 2001; Rice et al. 2003; Mejía et al. 2005). The actual value of C may vary depending on the physical conditions in the disk, e.g., C may depend on the disk thickness, chemical composition, dust content, etc. In the following text, we will refer to the dimensionless quantity $t_c \Omega$ as the \mathcal{G} -parameter and adopt $\mathcal{G} = 1$ as a fiducial critical value.

2. The Toomre criterion $Q = c_s \Omega / (\pi G \Sigma)$ for a Keplerian disk is smaller than some critical value Q_{cr} ,

usually taken to be unity (Toomre 1964). Here again, Q_{cr} may depend on the physical conditions and may vary by a factor of unity. The Toomre criterion implies that the gas surface density Σ should be sufficiently high for a disk to fragment. This criterion, along with $\mathcal{G} \leq 1-3$, is often invoked when analyzing the disk susceptibility to fragmentation (e.g. Rafikov 2005). There is, however, a catch—too high Σ may prevent fragmentation due to increased opacity and cooling time (Nero & Bjorkman 2009). In other words, there exists minimum and maximum values of Σ between which the instability and fragmentation are expected to occur. This means that any numerical simulation that starts from a *pre-defined* star/disk system with some disk-to-star mass ratio may run the risk of not revealing disk fragmentation if the initial Σ is too high. This is generally not a problem in numerical simulations that form disks self-consistently (such as our own), because during the disk formation phase Σ naturally increases from low toward higher values and the disk may pass through the unstable phase.

3. The amount of rotation in the natal cloud core should be sufficiently large in order to form extended and massive protostellar disks (Vorobyov & Basu 2006; Kratter et al. 2008; Vorobyov 2009b; Rice et al. 2010; Machida et al. 2010).
4. The time-averaged rate of mass accretion onto the disk ($\langle \dot{M}_d \rangle$) is greater than the time-averaged mass accretion onto the star ($\langle \dot{M}_* \rangle$) so that Σ quickly increases with time and may reach the unstable regime (Vorobyov & Basu 2006, 2007; Vorobyov 2009b; Kratter et al. 2010; Boley 2009).

We analyze the significance of these four criteria for disk fragmentation using our reference model. Figure 2 shows a series of images of the gas surface density (in g cm^{-2} , log units) in the inner 1000 AU at different times since the formation of the central star. The disk begins to form at $t \approx 0.08$ Myr and by $t = 0.13$ Myr a well-developed spiral pattern and several dense clumps are clearly visible. The clumps are almost always located in the spiral arms, suggesting that they form via fragmentation of the densest and coldest arms. Most fragments, however, do not live long. They are driven into the disk inner regions and through the sink cell (and probably onto the star) but other fragments take their place. Some of them are massive enough to host mini-disks of their own. Typical fragment masses lie in a wide range from several Jovian masses to low- and intermediate mass brown dwarfs. The mass spectrum of the fragments depends on the disk and cloud core properties and may vary from model to model.

The disk slowly grows in mass and size due to mass loading from the envelope (most of which is off the spatial scale in Figure 2). The disk structure is rather irregular, particularly in the early evolution. The gas velocity field in the bottom rows of Figure 2 reveals large non-circular motions, contractions, and expansions caused by ongoing angular momentum redistribution between the fragments

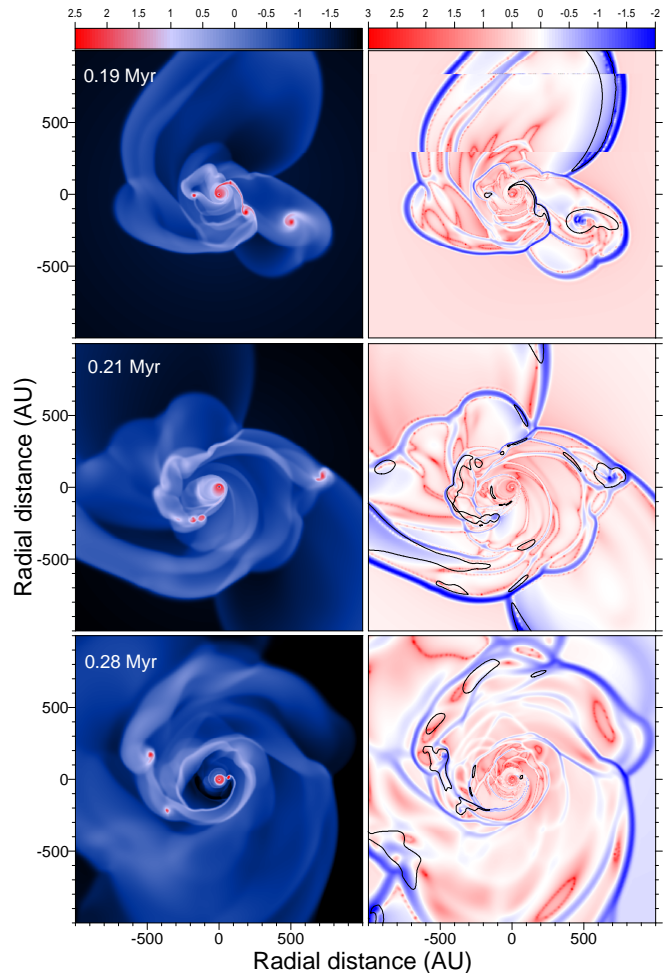


FIG. 3.— Gas surface density distribution (left column, g cm^{-2} , log units) and the spatial distribution of the \mathcal{G} -parameter (right column, log units) in the reference model at three typical times after the formation of the central star. Red contour lines comprise gravitationally unstable regions according to the Toomre criterion, $Q < 1$. Fragmentation is supposed to occur in the regions where $\mathcal{G} < 1$ and $Q < 1$ simultaneously.

and the rest of the disk (in particular, between the fragments and spiral arms). The disk in this early phase of evolution is most certainly *not* in a steady state and approximating the early disk evolution using a steady-state concept may be misleading.

Figure 2 reveals that the disk in the reference model is readily susceptible to fragmentation in the early evolution. How does the model comply with the four fragmentation criteria outlined above? Are all four conditions satisfied? We start with examining the importance of criteria 1 and 2 and search for any disk regions that are simultaneously characterized by both $Q < 1$ and $\mathcal{G} < 1$. Figure 3 presents several typical gas surface density distributions (left column, g cm^{-2} , log units) and the spatial distribution of the corresponding \mathcal{G} -parameter (right column, log units). In the latter case, those regions that cool sufficiently fast for fragmentation to take place ($\mathcal{G} < 1$) are plotted with blue, while slowly cooling regions with $\mathcal{G} > 1$ are plotted with red. Disk regions shown with white are near the border of stability, $\mathcal{G} = 1$. The black contour lines delineate the regions of the disk that are prone to fragmentation according to the Toomre criterion, $Q < 1$. It is clearly seen that *there are* regions in

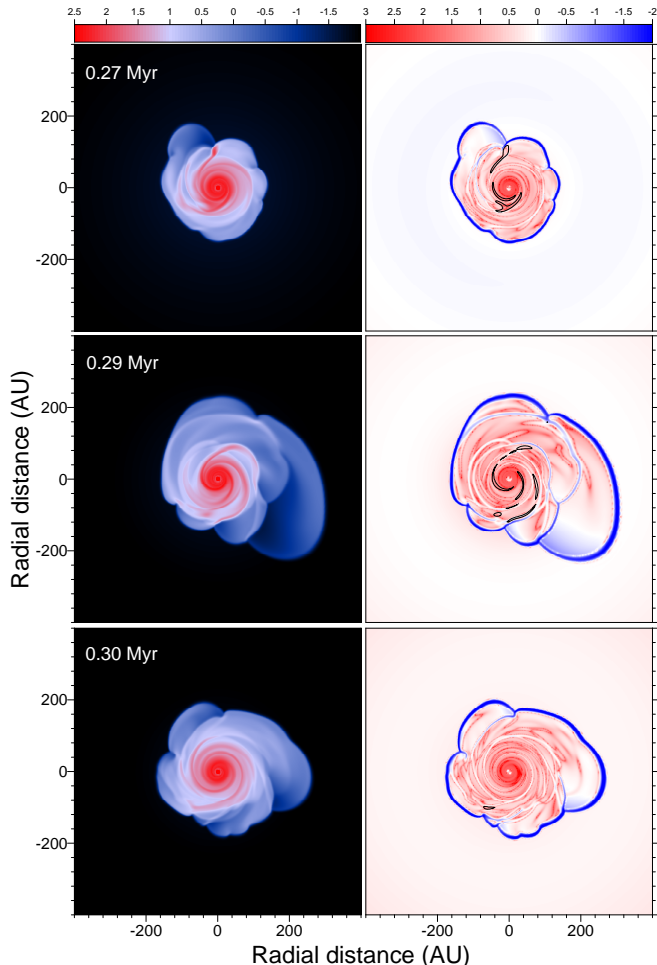


FIG. 4.— Same as in Figure 3 but for the lower- β model, $\beta = 2.8 \times 10^{-3}$. Note the lack of fragmentation.

the disk where the first two criteria for fragmentation, $\mathcal{G} \equiv t_c \Omega < 1$ and $Q < 1$, are fulfilled simultaneously. These are the fragments, especially those located in the outer disk regions, and certain parts of the spiral arms. It is seen that favorable sites for fragmentation lie preferably at large radii, implying that many fragments form at $r \gtrsim 100$ AU from the star but are driven later in the inner regions via exchange of angular momentum with the disk and, especially, with the spiral arms. This migration phenomenon⁴ was demonstrated by us in the context of barotropic disks (Vorobyov & Basu 2006).

Figure 3 demonstrates that criteria 1 and 2 for disk fragmentation are fulfilled in the reference model. What about the other two criteria? Criterion 3 is essentially an *initial condition* imposed on the cloud core which states that the rate of cloud core rotation should be sufficiently high for disk fragmentation to take place. To investigate the importance of this condition, we consider another model that is similar to the reference model but has a smaller initial rotation rate (hereafter, lower- β model). In particular, we set the ratio of rotational to gravitational energy to $\beta = 2.8 \times 10^{-3}$ (in contrast to $\beta = 1.3 \times 10^{-2}$ in the reference model) by decreasing the value of Ω_0 in Equation (13). The resulting distributions of the gas surface density Σ , \mathcal{G} -parameter, and

Toomre parameter Q are shown in Figure 4. The layout of the figure is the same as that of Figure 3 but the spatial scale is different. It is evident that the lower- β model has no well-defined fragments, though some transient density enhancements within the spiral arms are visible. The lack of disk fragmentation is not surprising—there are hardly any regions in the disk where criteria 1 and 2 are satisfied simultaneously. In fact, by $t = 0.3$ Myr, the disk lacks regions with $Q < 1$ and regions with $\mathcal{G} < 1$ are mostly located near the disk outer edge where intense cooling of the shocked gas (due to accretion from the envelope) takes place.

There are two major factors that work against disk fragmentation in the lower- β model. First, the disk size is considerably smaller than that of the reference model due to a smaller centrifugal radius $r_{\text{cf}} = \Omega^2 r^4 / GM(r)$. Smaller disks are subject to a stronger stabilizing influence of stellar irradiation. Second, the disk mass in the lower- β model is on average 20% smaller than that of the reference model, which also increases the disk stability against fragmentation in the lower- β model by raising the value of Q . In addition, small disks may be optically thick and thus cooling too slow to fragment (e.g. Rice et al. 2009; Clarke 2009).

The above analysis indicates that the initial conditions in a natal cloud core (in particular, the amount of rotation), are of considerable importance for the future disk evolution. In models with low β , the resulting disks are unlikely to fragment due to small disk sizes and masses. In this sense, criterion 3 is a necessary condition for disk fragmentation but not a sufficient one. As will be demonstrated later, disk propensity to fragment also depends on other factors such as magnetic fields, initial cloud core temperature and mass, etc. In this context, it is difficult to provide reliable estimates as to the exact amount of rotational energy (as specified, for example, by the ratio β of the rotational to gravitational energy) that a cloud core needs in order to produce disks capable for fragmentation. Therefore, we believe that providing any critical values of β for disk fragmentation may be misleading unless exact initial conditions in cloud cores are specified.

In the following section, we will consider mass accretion rates onto the disk and the star and discuss the significance of criterion 4 for disk fragmentation.

4. THE BURST MODE OF ACCRETION

Fragments that form in the disk pass through the sink cell as they migrate into the inner disk via exchange of angular momentum with the spiral arms. The ultimate fate of these fragments is uncertain and is largely dependent on how quickly they can contract from their initial size of several AU to a planetary size to avoid tidal destruction. The contraction time for a Jupiter-mass clump to reach a central temperature of 2000 K, i.e., the temperature required to dissociate H_2 to trigger rapid collapse, may be as long as a few $\times 10^5$ yr (Helled et al 2006). Considering a fast timescale of inward radial migration in the embedded phase—a few tens of orbital periods—we believe that most of these fragments⁵ will be tidally destroyed when approaching

⁴ The animation of this migration process can be downloaded at www.ap.smu.ca/~vorobyov/

⁵ The most massive fragments may survive and form giant planets or brown dwarfs on close orbits.

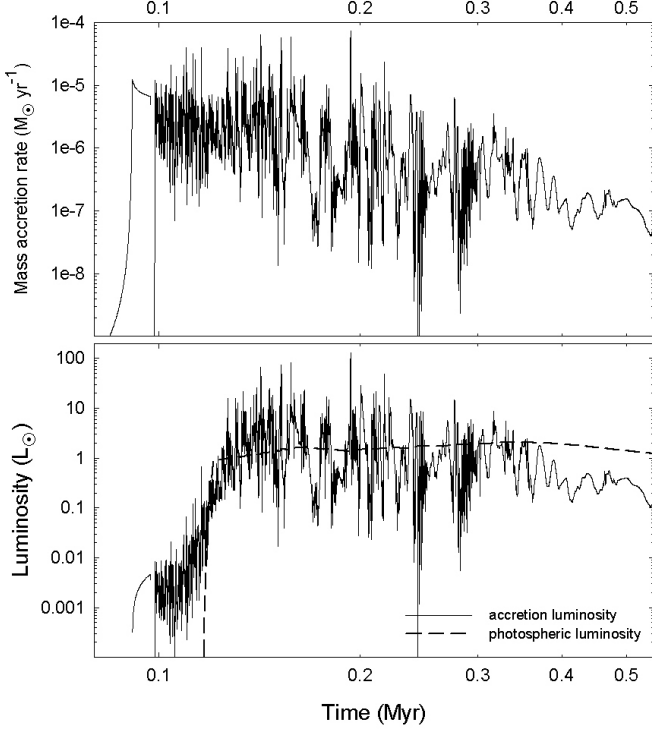


FIG. 5.— Mass accretion rate onto the star (top) and stellar luminosity (bottom) as a function of time elapsed since the beginning of collapse in the reference model. In particular, the solid and dashed lines in the bottom panel show the accretion and photospheric luminosities, respectively.

the central star, thus converting its gravitational energy to the accretion luminosity and producing an FU-Ori-like luminosity burst. This phenomenon is called the burst mode of accretion and it has been extensively studied by us for the case of barotropic disks (Vorobyov & Basu 2005, 2006). Here, we confirm that a more accurate treatment of disk thermodynamics does not qualitatively affect our earlier conclusions. However, as our recent simulations of barotropic disks have shown, some of the fragments that form in the late embedded phase may survive and evolve eventually into giant planets on wide orbits (Vorobyov & Basu 2010).

The instantaneous mass accretion rate from the disk onto the star \dot{M}_* is found in our model as the mass passing through the sink cell per one time step of integration (which in physical units is usually equal to 10–20 days). We also calculate the instantaneous mass accretion rate onto the disk from the infalling envelope \dot{M}_d as the mass passing (per one time step of integration) through a radial annulus located just outside the disk outer edge. Figure 5 presents the time evolution of the mass accretion rates and luminosities in the reference model. In particular, the top panel shows \dot{M}_* , while the bottom panel—accretion luminosity L_{accr} (solid line) and photospheric luminosity L_{ph} (dashed line).

In the pre-stellar phase, \dot{M}_* is negligible but quickly rises to $\approx 10^{-5} M_{\odot} \text{ yr}^{-1}$ when the gas volume density in the sink cell exceeds 10^{11} cm^{-3} and a central stellar core begins to form at $t \approx 0.08 \text{ Myr}$ after the onset of collapse. The subsequent short period of near-constant accretion corresponds to the phase when the infalling en-

velope lands directly onto the forming star⁶. A sharp drop in \dot{M}_* follows shortly, which manifests the beginning of the disk formation phase. Subsequently, the infalling envelope accretes onto the forming disk rather than directly onto the star. This transient drop in \dot{M} occurs due to the fact that the disk mass is initially too small to drive a substantial accretion rate onto the star either due to viscous or gravitational torques. As the evolution proceeds, the disk accretes mass from the infalling envelope and a qualitatively new phase of mass accretion ensues, in which \dot{M}_* shows variability by several orders of magnitude. Short episodes of high-rate accretion (caused by the passage of disk fragments through the sink cell) are followed by longer periods of low-rate accretion (caused by a temporary disk expansion and stabilization). This highly variable accretion makes the star sporadically increase its *total* luminosity, as illustrated in the bottom panel of Figure 5. Several clear-cut luminosity outbursts with L_{accr} as high as $100 L_{\odot}$ and many more weaker bursts (solid line) are evident against the background of a near-constant photospheric luminosity with $L_{\text{ph}} \sim 1.0 L_{\odot}$ (dashed line). The stronger bursts may represent FU Orionis-like eruptions, typical for the early evolution of a protostar, while weaker ones may manifest EX Lupi-like eruptions (EXors), typical for the later evolution. We note that the exact time for the onset of the photospheric luminosity is rather uncertain and may shift to later times (see discussion in Section 6), which would result in the early luminosity bursts being considerably stronger in amplitude.

We can now verify if our reference model complies with criterion 4 for disk fragmentation outlined in the previous section. This criterion requires that the rate of mass accretion onto the disk \dot{M}_d be *on average* greater than that onto the star \dot{M}_* . Figure 6 presents the time-averaged mass accretion rates onto the star $\langle \dot{M}_* \rangle$ (solid line) and onto the disk $\langle \dot{M}_d \rangle$ (dashed line) as a function of time since the beginning of collapse. The averaging is done over a period of 15000 yr. In the early evolution ($t < 0.2 \text{ Myr}$), $\langle \dot{M}_d \rangle$ is systematically greater than $\langle \dot{M}_* \rangle$ and this phase is characterized by the strongest burst activity. In the subsequent time period between 0.2 Myr and 0.3 Myr, both time-averaged accretion rates are of similar magnitude and the burst phenomenon persists, though with somewhat lesser frequency and amplitude. After $t = 0.4 \text{ Myr}$, $\langle \dot{M}_d \rangle$ becomes systematically lower than $\langle \dot{M}_* \rangle$ and the burst activity in this late phase diminishes. However, some small variations in \dot{M}_* persist even to later times.

Let us define the end of the embedded phase and the onset of the Class II phase of star formation as the time when the envelope empties, and its mass M_{env} drops below 5–10% of the initial cloud core mass M_{cl} . The vertical lines in Figure 6 correspond to the evolution times when $M_{\text{env}}/M_{\text{cl}} = 0.1$ (left) and $M_{\text{env}}/M_{\text{cl}} = 0.05$ (right). It is seen that $\langle \dot{M}_d \rangle \geq \langle \dot{M}_* \rangle$ in the Class 0 and I phases, while $\langle \dot{M}_d \rangle < \langle \dot{M}_* \rangle$ in the Class II phase. Hence, disk fragmentation and the associated burst phenomenon are likely to take place in *the embedded phase of star formation*, but

⁶ In fact, this period is expected to be even shorter since $r_{\text{sc}} \gg r_*$.

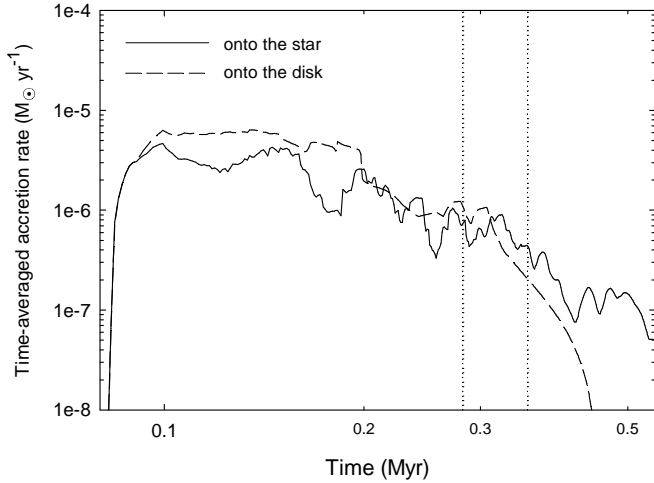


FIG. 6.— Time-averaged accretion rates onto the star (solid line) and onto the disk (dashed line) versus time since the onset of collapse in the reference model. The vertical dotted lines mark the onset of the Class II phase as inferred from the ratio of the envelope mass to the initial cloud core mass, 0.1 and 0.05 for the left and right lines, respectively

are unlikely later in the evolution simply because mass loading from the envelope diminishes in this phase.

Figure 6 demonstrates that criterion 4 is fulfilled in the reference model. Is this criterion sufficient for disk fragmentation to take place? In Figure 7 we present the instantaneous accretion rates \dot{M}_* (top panel) and time-averaged accretion rates (bottom panel) in the lower- β model introduced in the previous section. This model has a (roughly) five times smaller value of $\beta = 2.8 \times 10^{-3}$ as compared to that of the reference model and shows hardly any signs of disk fragmentation (see Figure 4). The lack of disk fragmentation manifests itself by a considerably weaker accretion variability than in the reference model—there are only order-of-magnitude flickering in \dot{M}_* and one moderate accretion burst. However, when we turn to the time-averaged accretion rates (bottom panel), we see that $\langle \dot{M}_{\text{env}} \rangle$ (dashed line) is actually greater than $\langle \dot{M}_* \rangle$ (solid line) in the EPSF, indicating that criterion 4 for disk fragmentation is fulfilled in the lower- β model. This example convincingly demonstrates that the fulfillment of criterion 4 is necessary but not sufficient for disk fragmentation to occur. The disk mass and radius in the lower- β model seem to be too small even in the case of a strong mass loading from the envelope.

5. THE EFFECT OF INITIAL CONDITIONS ON THE BURST MODE OF ACCRETION

In Section 3, we have already demonstrated the importance of rotation for the development of the burst mode of accretion in the early phases of stellar evolution. In this section, we study the effect that other initial conditions in collapsing cloud cores (such as cloud core mass and temperature, magnetic fields, etc.) may have on the strength and frequency of the bursts.

5.1. Initial cloud core mass

There is at least one good reason to believe that the initial mass of a cloud core should have a significant effect on the subsequent disk evolution—more massive cloud cores are expected to form more massive disks. This

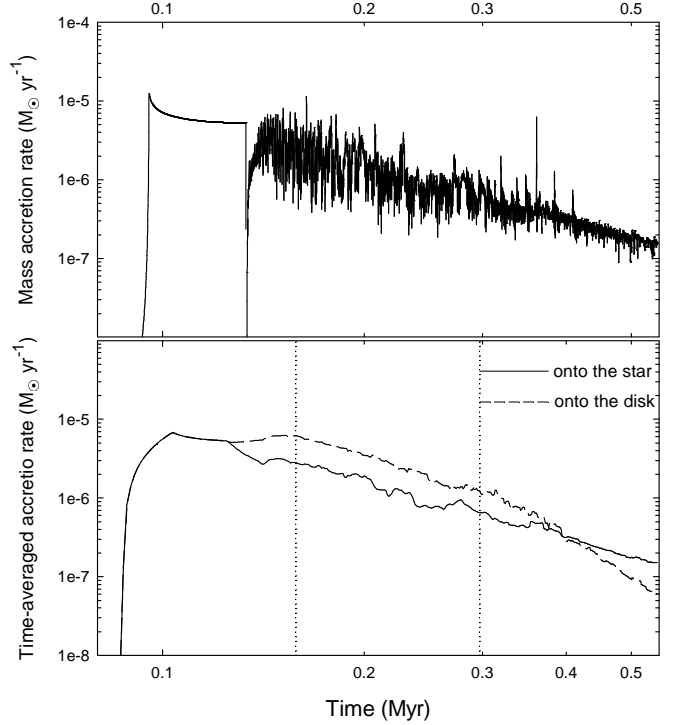


FIG. 7.— Instantaneous mass accretion rate (top) and time-averaged mass accretion rates (bottom) in the lower- β model, which is characterized by a five times lower $\beta = 2.8 \times 10^{-3}$ than that of the reference model. In particular, the solid and dashed lines in the bottom panel show the time-averaged accretion rates onto the star and onto the disk, respectively. Vertical dotted lines mark the onset of the Class I (left) and Class II (right) phases.

is simply because more massive cloud cores have larger sizes⁷ and, as a consequence, larger centrifugal radii r_{cf} for any reasonable radial mass distribution. Hence, we can expect disks formed from more massive cloud cores to have a higher tendency for fragmentation and a stronger accretion variability. This effect has been confirmed in the context of barotropic disks (Vorobyov & Basu 2006; Vorobyov 2009b). A similar tendency was demonstrated by Kratter et al. (2008), who showed that stars of greater mass tend to have disks that are more susceptible to fragmentation.

Figure 8 presents the mass accretion rates onto the star (left column) and accretion and photospheric luminosities (right column) in three models with $M_{\text{cl}} = 0.16 M_{\odot}$ (top row), $M_{\text{cl}} = 0.23 M_{\odot}$ (middle row), and $M_{\text{cl}} = 0.92 M_{\odot}$ (bottom row). In the following text, we refer to these models as the $M_{\text{cl}} = 0.16 M_{\odot}$ model, $M_{\text{cl}} = 0.23 M_{\odot}$ model, and $M_{\text{cl}} = 0.92 M_{\odot}$ model, respectively. Other parameters of these models are identical to the parameters of the reference model and are summarized in Table 1. It is seen that models with lower M_{cl} are characterized by a lower accretion variability, suggesting that the disk propensity to fragment declines with decreasing cloud core mass. The $M_{\text{cl}} = 0.16 M_{\odot}$ model exhibits hardly any (or very weak) accretion and luminosity bursts, with the photospheric luminosity dominating the total radiation flux for most of the evolution. The burst mode becomes prominent in the $M_{\text{cl}} = 0.23 M_{\odot}$ model, which shows three well-defined lu-

⁷ A cloud core may also increase its mass via density enhancement.

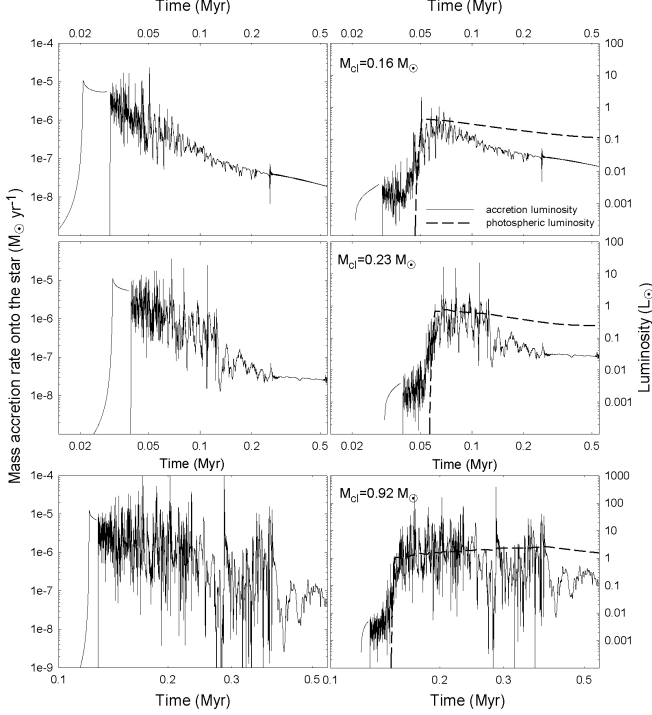


FIG. 8.— Mass accretion rate onto the star (left column) and stellar luminosity (right column) as a function of time since the beginning of collapse in the $M_{cl} = 0.16 M_{\odot}$ model (top), $M_{cl} = 0.23 M_{\odot}$ model (middle), and $M_{cl} = 0.92 M_{\odot}$ model (bottom). In particular, the solid and dashed lines in the bottom panel show the accretion and photospheric luminosities, respectively.

minosity outbursts. As the cloud core mass continues to increase, the burst frequency and intensity also increase and the $M_{cl} = 0.92 M_{\odot}$ model demonstrates multiple luminosity outbursts with $L_{accr} \sim 10\text{--}100 L_{\odot}$ and several ones with $L_{accr} > 100 L_{\odot}$, indicating the onset of vigorous gravitational instability and disk fragmentation.

We point out that all three models have the same value of $\beta = 1.3 \times 10^{-2}$, yet the $M_{cl} = 0.16 M_{\odot}$ and $M_{cl} = 0.23 M_{\odot}$ models have a considerably weaker burst activity than the $M_{cl} = 0.92 M_{\odot}$ model. This example demonstrates the importance of the initial cloud core mass for the development of disk fragmentation and associated burst mode of accretion. For disk fragmentation to take place, it is not sufficient for a cloud core to have a high initial rate of rotation—the initial cloud core mass should also be sufficiently high. We also note that as M_{cl} increases in Figure 8, the resulting total luminosity also increases but this does not suppress disk fragmentation. The growing disk mass outweighs the stabilizing influence of stellar irradiation, at least for stars with $M_{*} \lesssim 1.0 M_{\odot}$. Our conclusion is in line with that of Rice et al. (2010) who argue that the primary requirement for disk fragmentation is large enough β to produce disks with radii large enough for fragmentation. Indeed, we may form disk of greater size not only by increasing β but also by taking a larger (and hence more massive) cloud core.

5.2. Higher initial cloud core temperature

In the reference model, we set the initial cloud core temperature to $T_{init} = 10$ K. According to our model assumptions, this value is physically determined by the temperature of the background blackbody radiation T_{bg} ,

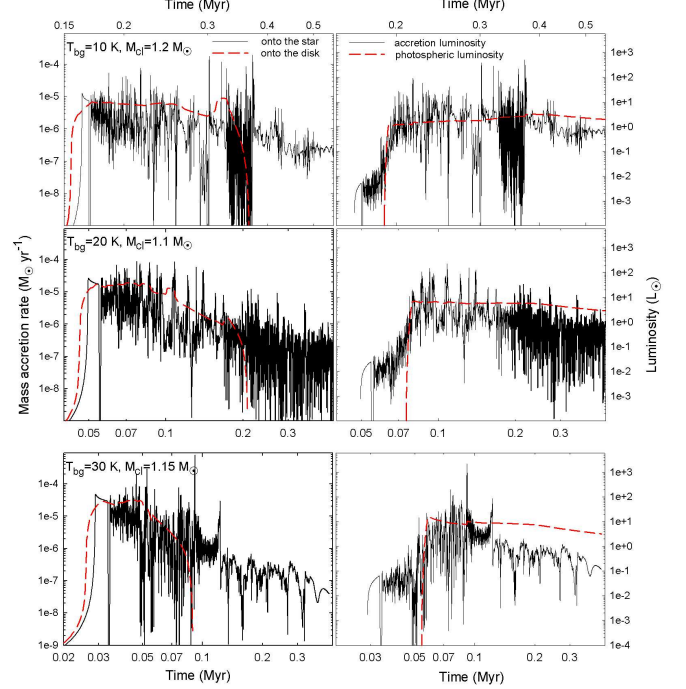


FIG. 9.— Mass accretion rates (left column) and stellar luminosity (right column) as a function of time since the beginning of collapse in the $T_{bg}=10$ K model (top), $T_{bg}=20$ K model (middle), and $T_{bg}=30$ K model (bottom). In particular, the black solid and red dashed lines in the left column present the instantaneous mass accretion rate onto the star and time-averaged mass accretion rate onto the disk, respectively, while these lines in the right column show the accretion and photospheric luminosities, respectively. A color version of this figure is available in the online journal.

i.e., $T_{init} = T_{bg}$. However, T_{bg} may be higher and this may influence the subsequent evolution of the cloud core in at least three ways. First, the rate of mass accretion onto the disk will be greater because \dot{M}_d is proportional to the cube of the sound speed. This effect will assist disk fragmentation. Second, the background radiation flux will grow and moderate the disk tendency to fragment by systematically increasing the disk temperature (Cai et al. 2008). And lastly, an increased rate of mass accretion onto the disk may eventually lead to an increased rate of mass accretion onto the star, thus raising the accretion luminosity and contributing to another factor against disk fragmentation. It is unclear a priori which of the three key factors would dominate the disk evolution.

To study the effect of varying background temperature, we consider three models that have similar cloud core masses and rotation rates but different background temperatures: $T_{bg} = 10$ K, $T_{bg} = 20$ K, and $T_{bg} = 30$ K. In the following text, we refer to these models as the $T_{bg} = 10$ K model, $T_{bg} = 20$ K model, and $T_{bg} = 30$ K model, respectively, and their parameters are listed in Table 1. We specifically choose models with similar M_{cl} and β in order to avoid any possible interference with the effects based on different cloud core masses and rotation rates considered in Section 4 and 5.1, respectively. Figure 9 presents mass accretion rates (left column) and luminosities (right column) as a function of time since the onset of gravitational collapse in the $T_{bg}=10$ K model (top row), $T_{bg}=20$ K model (middle row) and $T_{bg}=30$ K model (bottom panel). In particular, the black solid and red dashed

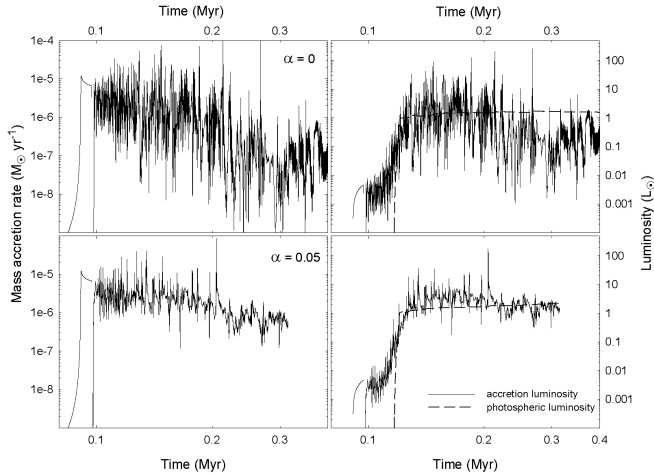


FIG. 10.— Mass accretion rates onto the star (left column) and stellar luminosity (right column) as a function of time since the beginning of collapse in the $\alpha = 0$ model (top) and $\alpha = 0.05$ model (bottom). In particular, the solid and dashed lines in the right column present the accretion and photospheric luminosities, respectively.

line in the left column are the instantaneous mass accretion rate onto the star \dot{M}_* and the time-averaged (over 15000 yr) mass accretion rate onto the disk $\langle \dot{M}_d \rangle$, respectively. The black solid and red dashed lines in the right column are the accretion and photospheric luminosities, respectively.

A comparison of the three models reveals that the $T_{\text{bg}}=20$ K model exhibits a vigorous burst activity comparable in strength and frequency to that of the $T_{\text{bg}}=10$ K model. However, the duration of the burst phase appears to be shorter in the higher- T_{bg} model. As we further increase the background temperature to $T_{\text{bg}}=30$ K, the burst activity decreases notably, yet there are two well-defined accretion and luminosity outbursts that reveal the disk is still prone to fragmentation. In fact, the magnitude of these bursts is much stronger than in the lower- T_{bg} models, indicating that a higher background radiation favors the formation of more massive fragments (though in a much smaller quantity). As was expected from theoretical grounds, the photometric luminosity $L_{*,\text{ph}}$ is greater in models with higher T_{bg} , but so is the mass accretion rate onto the disk $\langle \dot{M}_d \rangle$ (at least in the early phase). It appears that an elevated mass accretion rate onto the disk outweighs the stabilizing influence of the background and stellar irradiation. We conclude that protostellar disks illuminated by the background irradiation with temperatures of the order of 30 K (and probably higher) are still prone to fragmentation and development of the burst mode of accretion.

5.3. The effect of viscosity

The effect of disk viscosity on the burst mode of accretion was studied by us in the context of barotropic disks (Vorobyov & Basu 2009a). For the usual α -parameterization of Shakura & Sunyaev (1973) and temporally and spatially constant α , disks with lower values of α are disposed to stronger fragmentation and demonstrate a stronger burst mode of accretion. In addition, the accretion variability also increases along the line of decreasing α (Vorobyov & Basu 2009a; Vorobyov 2009b).

In all models considered so far, we have adopted $\alpha =$

0.005. To see how different values of α could affect our conclusions, we run two models with $\alpha = 0$ and $\alpha = 0.05$ but other parameters identical to those of the reference model (see Table 1). Figure 10 presents the mass accretion rates onto the star (left column) and luminosities (right column) in the $\alpha = 0$ model (top row) and $\alpha = 0.05$ model (bottom row). As expected, the $\alpha = 0$ model demonstrates a vigorous burst activity, while the $\alpha = 0.05$ model shows only one strong luminosity outburst with L_{accr} in excess of $100 L_\odot$, with other outbursts characterized by $L_{\text{accr}} \lesssim 20 L_\odot$. We confirm that a factor of 10 increase in α does not suppress disk fragmentation completely. However, an additional strong source of mass transport via viscous torques reduces the disk mass and this acts to moderate the disk propensity to fragment.

The problem with the $\alpha = 0.05$ model is that it demonstrates hardly any accretion episodes with $\dot{M}_* < 10^{-6} M_\odot \text{ yr}^{-1}$ in the early 0.2 Myr of evolution. The lack of low-rate accretion in disks with $\alpha > 0.01$ was also found in the context of barotropic disks (Vorobyov & Basu 2009a; Vorobyov 2009b) and this confronts recent observations of Enoch et al. (2009), who find that a considerable fraction of Class I sources in young star-forming regions have inferred accretion rates below $10^{-6} M_\odot \text{ yr}^{-1}$. We note that both the $\alpha = 0$ and $\alpha = 0.005$ models show plenty of such low-accretion episodes. We therefore argue that disk viscosity in the embedded phase is unlikely to be characterized by $\alpha \gtrsim 0.01$.

In a broader context of viscous ($\alpha < 0.01$) versus non-viscous ($\alpha = 0$) models, the former seem to yield accretion rates in the Class II (or T Tauri) phase that are a factor 2–3 greater than those of the non-viscous model (Vorobyov & Basu 2007, 2008). As a result, an addition of α -transport helps to bring Class II disk masses in better agreement with observations (Vorobyov 2009a). On the other hand, the early disk evolution (Class 0 and I phases) is weakly affected by α -viscosity because mass and angular momentum transport in this stage is largely dominated by gravitational torques (Vorobyov & Basu 2009a). This can also be seen from the comparison of Figure 5 with the top panels of Figure 10—there is little *qualitative* difference in the mass accretion history between the $\alpha = 0$ and $\alpha = 0.005$ models in the EPSF.

6. MODEL LIMITATIONS

In this section, we discuss several assumptions in our model that can potentially influence our results. 1) *The onset of photospheric luminosity.* As was discussed in Section 2.3, the stellar age in D’Antona & Mazitelli’s (1997) pre-main sequence evolution tracks is difficult to relate to the physical evolution time in numerical simulation of cloud core collapse. We have equated their zero-point time to the time when the second atomic core presumably starts to form in our numerical simulations. This may be a *conservative* assumption. In D’Antona & Mazitelli models, the evolution generally begins from a central temperature of $\log(T_c) = 5.7$, i.e., at a time instance just preceding deuterium burning, and it may take some time for the forming second core to ignite deuterium burning in its interior. Hence, the photospheric luminosity may turn on somewhat later than assumed in our numerical simulations and this could actually act to increase the disk susceptibility to fragmentation.

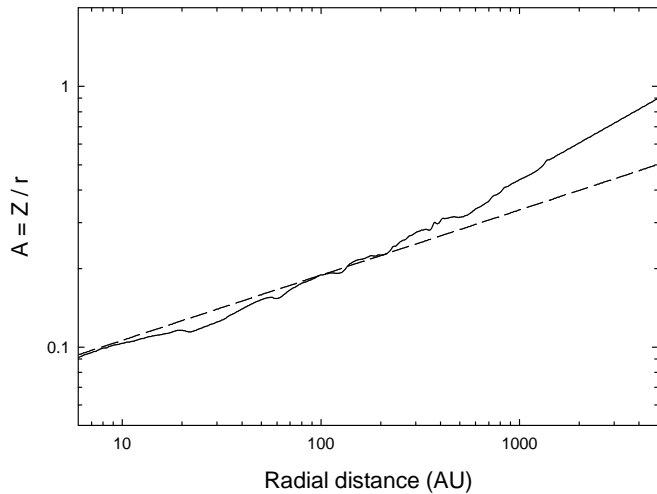


FIG. 11.— Aspect ratio A of the disk vertical scale height to radius (Z/r) as a function of radius (r). The thick solid line shows A in the reference model at $t = 0.19$ Myr after the formation of the central star. The dashed line presents the aspect ratio derived from the following expression $Z/r = 0.1(r/100 \text{ AU})^{0.25}$, as suggested by detailed disk vertical structure modeling by D'Alessio et al. (1999).

2) *Accretion rate onto the star.* In our models, the size of the sink cell $r_{\text{sc}} = 6$ AU is larger than the stellar radius. The inner disk at $r < 6$ AU may add additional variability to the accretion rates, in particular due to the thermal instability (Bell & Lin 1994) or magneto-rotational instability (Armitage et al. 2001; Zhu et al. 2009). These effects may somewhat alter the temporal behavior of the actual accretion rates onto the stellar surface and affect the accretion luminosity. However, our accretion rates are in good accord with those inferred for nearby star-forming regions and we believe that the actual accretion rates onto the stellar surface are not substantially different from those calculated in our modeling.

3) *Jet efficiency.* Protostellar jets may evacuate a substantial fraction of the accreting material, reducing the effective mass of the star as compared to the case without jets. In our modeling, we set the jet efficiency to 10%, which means that the stellar mass is systematically lower by 10% than that of the non-jet case. This in fact promotes gravitational instability in the disk as the disk-to-star mass ratio is increased accordingly. However, the jet efficiency may be higher and amount to 30% and possibly more (e.g., Shu et al. 1999). This would act to further destabilize the disk.

4) *Stellar wobbling.* The position of the central star in our models is fixed in the coordinate center. However, the star may move in response to the non-axisymmetric gravitational field of the disk. Semi-analytic considerations suggest that this stellar wobbling may amplify gravitational instability in the disk (Adams et al. 1989), though the recent numerical hydrodynamics simulations find this effect insignificant (Scott & Durisen 2010). To implement such a mechanism in our models is however not easy due to the presence of singularity in the coordinate center on the polar grid. We plan to explore the effect of stellar wobbling in a future study.

5) *Binary or multiple system formation.* In addition to the clump formation that we see in the present models, we have also seen the formation of a binary companion (or multiple companions) in the outer disk in models with $M_{\text{cl}} \gtrsim 1.7 M_{\odot}$ and $\beta \gtrsim 2.0 \times 10^{-2}$. These models will

be presented in a future paper. We note that to fully capture binary formation in the outer regions with our logarithmic grid, we need even higher numerical resolution than in the present study.

5) *Magnetic fields.* Frozen-in magnetic fields moderate the burst activity due to an effective increase in the Q -parameter (Vorobyov & Basu 2006). For a spatially and temporally uniform mass-to-flux ratio, the magnetic tension acts as a simple dilution of gravity, thus effectively lowering the disk surface density, and the magnetic pressure is a multiple of the gas pressure, thus providing an effective increase to the disk sound speed. A more comprehensive study of the effect of magnetic fields, including ambipolar diffusion and magnetic braking, is planned for a future paper.

7. CONCLUSIONS

We have revisited our original results on the burst mode of accretion (Vorobyov & Basu 2005, 2006), paying special attention to the thermal processes in protostellar disks around low-mass protostars. Our new model takes into account radiative cooling from the disk surface, viscous and shock heating, and also stellar and background irradiation. Thanks to the use of the thin-disk approximation, we can run uninterrupted numerical hydrodynamics simulations from the prestellar phase to the early T Tauri phase, fully capturing the embedded phase of star formation (EPSF). We find the following.

- The EPSF is likely the only episode of disk evolution when disk fragmentation can take place. However, disk susceptibility to fragmentation in this phase depends crucially on the *initial conditions* in a natal cloud core.
- Higher initial core angular momentum and mass lead to the formation of more massive and extended disks and, therefore, favor disk fragmentation. On the other hand, a higher temperature of the background irradiation T_{bg} may moderate the disk propensity to fragment. In particular, higher T_{bg} appears to favor the formation of more massive fragments though in much fewer numbers.
- A higher rate of mass infall onto the disk than that onto the star in the EPSF does not guarantee disk fragmentation if the disk is not sufficiently large and massive.
- For disk fragmentation to occur, *both* the Toomre Q -parameter and \mathcal{G} -parameter (ratio of the local cooling time to the dynamical time) must be below some critical value, taken to be unity in this paper, confirming many previous studies on disk instability and fragmentation.
- Most (but possibly not all) fragments that form in the EPSF are driven into the inner disk regions and probably onto the star, triggering mass accretion and luminosity bursts similar in magnitude to those of the FU-Orionis-type and EX-Lupi-like stars. This burst mode of accretion is a robust phenomenon that is expected to exist in a variety of environments and for a variety of systems with different physical properties. The intensity of the

burst mode correlates with the disk propensity to fragment.

- Fragmenting disks drive highly variable accretion rates onto the star ranging from $10^{-8} M_{\odot} \text{ yr}^{-1}$ to $10^{-4} M_{\odot} \text{ yr}^{-1}$. Protostellar disks that are gravitationally unstable but stable to fragmentation are characterized by a considerably weaker accretion variability with only an order of magnitude flickering.
- The intensity of the burst mode of accretion is sensitive to the amount of α -viscosity present in protostellar disks and appears to subside with increasing α . The lack of strong variability in disks with a spatially and temporally uniform $\alpha \gtrsim 0.05$ contradicts

observations (e.g. Enoch et al. 2009) and renders such disk not viable.

E.I.V. gratefully acknowledges present support from an ACEnet Fellowship, RFBR grant 10-02-00278, and Ministry of Education grant RNP 2.1.1/1937. Numerical simulations were done on the Atlantic Computational Excellence Network (ACEnet), on the Shared Hierarchical Academic Research Computing Network (SHARCNET), and at the Center of Collective Supercomputer Resources, Taganrog Technological Institute at Southern Federal University. S. B. was supported by a Discovery Grant from the Natural Sciences and Engineering Research Council of Canada.

APPENDIX

A. THE THIN-DISK APPROXIMATION

The thin-disk approximation is well justified as long as the aspect ratio $A = Z/r$ of the disk vertical scale height Z to radius r does not considerably exceed 0.1. In a Keplerian disk, $Z = c_s/\Omega$ and noticing that the angular velocity is $\Omega = (GM_*/r^3)^{1/2}$ and the sound speed is $c_s \leq Q_{\text{cr}}\pi G\Sigma/\Omega$, the aspect ratio can be expressed as

$$A \leq \frac{Q_{\text{cr}} M_{\text{d}}(r)}{CM_*}, \quad (\text{A1})$$

where $M_{\text{d}}(r) = \int \Sigma(r, \phi) r dr d\phi$ is the disk mass contained within radius r , M_* is the mass of the central star, Q_{cr} is the critical Toomre parameter, and C is a constant, the actual value of which depends on the gas surface density distribution Σ in the disk. For a disk of constant surface density, C is equal unity. However, circumstellar disks are characterized by surface density profiles declining with radius. For the scaling $\Sigma \propto r^{-1.5}$ typical for our disks, $C = 4$. Adopting further $Q_{\text{cr}} = 2$ and $M_{\text{d}}(r)/M_* = 0.5$, which are typical *upper* limits in our numerical simulations, we obtain $A \lesssim 0.25$. This analysis demonstrates that the thin-disk approximation is certainly valid in the inner regions where $M_{\text{d}}(r)/M_*$ is small, but may become only marginally valid at large r where $M_{\text{d}}(r)/M_*$ would approach its maximum value.

The azimuthally-averaged radial distribution of the aspect ratio $A = Z/r$ in the reference model at $t = 0.19$ Myr after the formation of the central star is shown by the solid line Figure 11. The vertical scale height Z is calculated assuming a local vertical hydrostatic equilibrium in the disk using the method described in Vorobyov & Basu (2009a). Figure 11 reinforces our analytical estimates and demonstrates the thin-disk approximation is certainly obeyed in the disk. Our disks rarely exceed 1000 AU in radius and the corresponding aspect ratio is kept in the 0.1–0.4 limits. Only at radial distances well in excess of 1000 AU may the thin-disk approximation be violated.

B. RADIATION FLUX FROM THE CENTRAL STAR

In order to calculate the radiation flux from the central star F_{irr} at a given radial distance r using Eq. (9), one needs to know the incidence angle of radiation arriving at the disk surface γ_{irr} (i.e., the angle between the light rays and the perpendicular to the disk surface). For a flaring disk, the cosine of γ_{irr} can be expressed as

$$\cos \gamma_{\text{irr}} = \cos \alpha_{\text{irr}} \cos \beta_{\text{irr}} (\tan \alpha_{\text{irr}} - \tan \beta_{\text{irr}}), \quad (\text{B1})$$

where $\cos \alpha_{\text{irr}} = dr/(dr^2 + dZ^2)^{1/2}$, $\cos \beta_{\text{irr}} = r/(r^2 + Z^2)^{1/2}$, $\tan \alpha_{\text{irr}} = dZ/dr$, and $\tan \beta_{\text{irr}} = Z/r$. In most cases, $\cos \alpha_{\text{irr}} \approx 1$ and $\cos \beta_{\text{irr}} \approx 1$, since $Z/r \ll 1$ (thin disk) and $dZ/dr \ll 1$ (weak flaring). Nevertheless, we use the complete expression for $\cos \gamma_{\text{irr}}$.

In the reality, the disk surface may not always be of the concave shape, so that $\tan \alpha_{\text{irr}} - \tan \beta_{\text{irr}} > 0$ and $F_{\text{irr}} > 0$. If the shape of the disk surface becomes convex, i.e., $\tan \alpha_{\text{irr}} - \tan \beta_{\text{irr}} < 0$, the irradiation flux F_{irr} becomes negative. Physically, this corresponds to the situation when part of the disk surface is shielded from the incoming radiation from the central star, for instance, by a local puffing of the disk. This may be potentially an important phenomenon. However, taking this effect into account self-consistently may require the use of full radiation transfer using ray tracing and is out of scope of the present paper. Therefore, to avoid this complication, we make use of the detailed vertical structure models of irradiated accretion disks around T Tauri stars by D'Alessio et al. (1999). From their figure 1(b) (dashed curve) we have derived the following expression $Z/r = 0.1(r/100 \text{ AU})^{0.25}$ for the aspect ratio Z/r as a function of radial distance r , where 0.1 is the ratio Z/r at $r = 100$ AU and exponent 0.25 determines the degree of disk flaring (for positive/negative exponents, the disk surface is concave/convex, respectively). We adopt this relation with a modification according to our model, i.e., we actually calculate the aspect ratio Z/r at 100 AU using the azimuthally averaged value of the vertical scale height Z . This would allow us to dynamically adjust the aspect ratio Z/r according to the actual disk thickness but keep the disk shape concave throughout the simulation.

Another effect that has to be taken into account is the attenuation of stellar irradiation by the infalling envelope in the embedded phase of star formation (EPSF). This is done by introducing a factor A_{irr} in Eq. (9) calculated as $A_{\text{irr}} = M_{\text{cl}}/(M_{\text{env}} + M_{\text{cl}})$, where M_{cl} is the cloud core mass (stays fixed) and M_{env} is the gradually decreasing envelope mass. In the early EPSF, $M_{\text{cl}} \approx M_{\text{env}}$ and $A_{\text{irr}} \approx 0.5$, while in the late EPSF, $M_{\text{env}} \rightarrow 0$ and $A_{\text{irr}} \rightarrow 1$.

C. SUPPLEMENTARY MATHEMATICAL FORMULA

For the convenience of the reader and for completeness, we provide the actual expressions for $(\nabla \cdot \mathbf{\Pi})_p$, $(\nabla \mathbf{v})_{pp}$, and $[\nabla \cdot (\Sigma \mathbf{v}_p \otimes \mathbf{v}_p)]_p$ used in our paper. The components of $\nabla \cdot \mathbf{\Pi}$ in polar coordinates (r, ϕ) are

$$(\nabla \cdot \mathbf{\Pi})_r = \frac{1}{r} \frac{\partial}{\partial r} r \Pi_{rr} + \frac{1}{r} \frac{\partial}{\partial \phi} \Pi_{r\phi} - \frac{\Pi_{\phi\phi}}{r}, \quad (\text{C1})$$

$$(\nabla \cdot \mathbf{\Pi})_\phi = \frac{\partial}{\partial r} \Pi_{\phi r} + \frac{1}{r} \frac{\partial}{\partial \phi} \Pi_{\phi\phi} + 2 \frac{\Pi_{r\phi}}{r}, \quad (\text{C2})$$

where we have neglected the contribution from off-diagonal components Π_{rz} and $\Pi_{\phi z}$. The components of the viscous stress tensor $\mathbf{\Pi}$ in polar coordinates (r, ϕ) can be found from Eq. (6) according to the usual rules.

When calculating the symmetrized velocity gradient tensor $\nabla \mathbf{v}$, only the following planar components are assumed to be non-zero:

$$(\nabla \mathbf{v})_{rr} = \frac{\partial v_r}{\partial r}, \quad (\text{C3})$$

$$(\nabla \mathbf{v})_{r\phi} = \frac{1}{r} \frac{\partial v_r}{\partial \phi} + \frac{\partial v_\phi}{\partial r} - \frac{v_\phi}{r}, \quad (\text{C4})$$

$$(\nabla \mathbf{v})_{\phi\phi} = \frac{1}{r} \frac{\partial v_\phi}{\partial \phi} + \frac{v_r}{r}. \quad (\text{C5})$$

The symmetric dyadic $\Sigma \mathbf{v}_p \otimes \mathbf{v}_p$ is a rank-two tensor expressed in polar coordinates (r, ϕ) as

$$\Sigma \mathbf{v}_p \otimes \mathbf{v}_p = \begin{vmatrix} \Sigma v_r v_r & \Sigma v_r v_\phi \\ \Sigma v_\phi v_r & \Sigma v_\phi v_\phi \end{vmatrix}. \quad (\text{C6})$$

The planar components of $[\nabla \cdot (\Sigma \mathbf{v}_p \otimes \mathbf{v}_p)]_p$ can then be found using Eqs. (C1) and (C2) with $\mathbf{\Pi}$ substituted by $\Sigma \mathbf{v}_p \otimes \mathbf{v}_p$.

Finally, the viscous heating term $(\nabla \mathbf{v})_{pp'} : \Pi_{pp'}$ in the energy balance equation is the convolution of two rank-two tensors and its expression in the thin-disk approximation (neglecting the off-diagonal components) is as follows

$$(\nabla \mathbf{v})_{pp'} : \Pi_{pp'} = \frac{2\mu}{3} \left\{ (\nabla \mathbf{v})_{rr}^2 + (\nabla \mathbf{v})_{\phi\phi}^2 + [(\nabla \mathbf{v})_{rr} - (\nabla \mathbf{v})_{\phi\phi}]^2 \right\} + 2 (\nabla \mathbf{v})_{r\phi} \Pi_{r\phi}. \quad (\text{C7})$$

REFERENCES

- Andrews, S. M., & Williams, J. P. 2007, *ApJ*, 671, 1800
 Adams, F. C., Ruden, S. P., & Shu, F. H. 1989, *ApJ*, 347, 959
 Armitage, P. J., Livio, M., & Pringle, J. E. 2001, *MNRAS*, 324, 705
 Balbus, S. A., & Hawley, J. F. 1991, *ApJ*, 376, 214
 Basu, S. 1997, *ApJ*, 485, 240
 Bate, M. R. 2010, *MNRAS*, 4040, 79
 Bell, K. R., & Lin, D. N. C. 1994, *ApJ*, 427, 987
 Binney, J., & Tremaine, S. 1987, *Galactic Dynamics*, Princeton Univ. Press
 Boley, A. C. 2009, *ApJ*, 695, L53
 Bonnell, I., & Bastien, P. 1992, *ApJ*, 401, L31
 Cai, K., Durisen, R. H., Boley, A. C., Pickett, M. K., & Mejía, A. C. 2008, *ApJ*, 673, 1138
 Caselli, P., Benson, P. J., Myers, P. C., & Tafalla, M. 2002, *ApJ*, 572, 238
 Clarke, C. J. 2009, *MNRAS*, 396, 1066
 D'Alessio, P., Calvet, N., Hartmann, L., Lizano, S., & Canto, J. 1999, *ApJ*, 527, 893
 Dapp, W. B., & Basu, S. 2009, *MNRAS*, 395, 1092
 D'Antona, F., & Mazitelli, I. 1997, *Memorie della Societa Astronomia Italiana*, 68, 807
 Enoch, M. L., Evans, N. J., II, Sargent, A. I., & Glenn, J. 2009, *ApJ*, 692, 973
 Forgan, D., Rice, K., Stamatellos, D., Whitworth, A. 2009, *MNRAS*, 394, 882
 Forgan, D., & Rice, K. 2010, *MNRAS*, 402, 1349
 Gammie, C. F. 2001, *ApJ*, 553, 174
 Goodman, A. A., Benson, P. J., Fuller, G. A., & Myers, P. C. 1993, *ApJ*, 406, 528
 Hartmann, L., & Kenyon, S. J. 1996, *ARA&A*, 34, 207
 Helled, R., Podolak, M., & Kovetz, A. 2006, *Icarus*, 185, 64
 Herbig, G. H. 1977, *ApJ*, 217, 693
 Hubeny, I. 1990, *ApJ*, 351, 632
 Johnson, B. M., & Gammie, C. F. 2003, *ApJ*, 597, 131
 Kratter, K. M., Matzner, C. D., & Krumholz, M. R. 2008, *ApJ*, 681, 375
 Kratter, K. M., Matzner, C. D., Krumholz, M. R., & Klein, R. I. 2009, *ApJ*, 708, 1585
 Lin, D. N. C., & Papaloizou, J. C. B. 1985, in *Protostars and Planets II*, ed. D. C. Black & M. C. Matthews (Tucson, AZ: Univ. Arizona Press), 981
 Lissauer, J. J. 1993, *ARA&A*, 31, 129
 Lodato, G., & Clarke, C. J. 2004, *MNRAS*, 353, 841
 Machida, M. N., Inutsuka, S., & Matsumoto, T. 2010, *astro-ph:1001.1404*
 Masunaga, H., & Inutsuka, S. 2000, *ApJ*, 531, 350
 Mejía, A. C., Durisen, R. H., Pickett, M. K., & Cai, K. 2005, *ApJ*, 619, 1098
 Myers, P. C., Adams, F. C., Chen, H., & Schaff, E. 1998, *ApJ*, 492, 703
 Nero, D., & Bjorkman, J. E. 2009, *ApJ*, 702, L163
 Palla, F., & Stahler, S. W. 1991, *ApJ*, 375, 288
 Rafikov, R. R. 2007, *ApJ*, 621, L69
 Pfalzner, S., Tackenberg, J., & Steinhausen, M. 2008, *A&A*, 487, L45

- Rice, W. K. M., Armitage, P. J., Bate, M. R., & Bonnell, I. A. 2003, *MNRAS*, 339, 1025
- Rice, W. K. M., & Armitage, P. J. 2009, *MNRAS*, 396, 2228
- Rice, W. K. M., Mayo, J. H., & Armitage, P. J. 2010, 402, 1740
- Richtmeyer, R. D., & Morton, K. W. 1957, *Difference Methods for Initial-Value Problems*, 2d ed. (New York: Wiley Interscience)
- Scott, M., & Durisen, R. H. 2010, *MNRAS*, 406, 279
- Shakura, N. I., & Sunyaev, R. A. 1973, *A&A*, 24, 337
- Shu, F. H. 1977, *ApJ*, 214, 488
- Shu, F. H., Allen, A., Shang, H., Ostriker, E. C., & Li, Z.-Y. 1999, in *The Origin of Stars and Planetary Systems*, ed. C. J. Lada & N. Kylafis (Dordrecht: Kluwer), 193
- Stone, J. M., & Norman, M. L. 1992, *ApJS*, 80, 753
- Toomre, A. 1964, *ApJ*, 139, 1217
- Visser, R. van Dishoeck, E. F., Doty, S. D. & Dullemond, C. P. 2009, *A&A*, 495, 881
- Vorobyov, E. I. 2009a, *ApJ*, 692, 1609
- Vorobyov, E. I. 2009b, *ApJ*, 704, 715
- Vorobyov, E. I. 2010, *ApJ*, 713, 1059
- Vorobyov, E. I., & Basu, S. 2005, *ApJ*, 633, L137
- Vorobyov, E. I., & Basu, S. 2006, *ApJ*, 650, 956
- Vorobyov, E. I., & Basu, S. 2007, *MNRAS*, 381, 1009
- Vorobyov, E. I., & Basu, S. 2008, *ApJ*, 676, L139
- Vorobyov, E. I., & Basu, S. 2009a, *MNRAS*, 393, 822
- Vorobyov, E. I., & Basu, S. 2009b, *ApJ*, 703, 922
- Vorobyov, E. I., & Basu, S. 2010, *ApJ*, 714, L133
- Zhu, Z., Hartmann, L., & Gammie, C. F. 2009, *ApJ*, 694, 1045
- Zhu, Z., Hartmann, L., Gammie, C. F., Book, L. G., Simon, G. B., & Engelhard, E. 2010, *ApJ*, 713, 1134